Supporting information for

Microwave assisted $Gd(OH)_3$–MXene Nanocomposites for High Power Density Solid State Supercapacitor Applications

P. E. Lokhande,*[a] Dadaso D Mohite,[b] Amol Vedpathak,[c] Deepak Kumar,[d] Radhamanohar Aepuru,[e] Udayabhaskar Rednam,[f] Bandar Ali Al-Asbahi*[g]

[a]*Institute of Fundamental Technological Research, Polish Academy of Sciences, Pawińskiego 5B, 02-106 Warsaw, Poland*

[b]*Bharati Vidyapeeth (Deemed to be University) College of Engineering, Pune- 411043 (India)*

[c]*Symbiosis Centre for Nanoscience and Nanotechnology, Symbiosis International University, Lavale, Pune – 412 115, India*
[d]*Department of Chemistry, Manipal University, Jaipur, India*

[e]*Departamento de Ingeniería Mecánica, Facultad de Ciencias Físicas y Matemáticas, Universidad de Chile, Santiago, Chile*

[f]*Departamento de Mecánica, Facultad de Ingeniería, Universidad Tecnológica Metropolitana, Santiago, Chile*

[g6]*Department of Physics & Astronomy, College of Science, King Saud University, P.O. Box 2455, Riyadh 11451, Saudi Arabia*

Corresponding author: plokh@ippt.pan.pl

Characterization

The synthesized material was thoroughly examined to understand its structural, chemical, and morphological characteristics. X-ray diffraction (XRD) using Cu Kα radiation (λ = 1.5406 Å) verified its crystalline nature, phase purity, and the successful formation of the targeted oxide phases. Fourier-transform infrared spectroscopy (FTIR), recorded in the 4000–400 cm^{-1} range, identified the surface functional groups, showing bands corresponding to –OH stretching, residual nitrate species, and metal–oxygen vibrations. Scanning electron microscopy (SEM) revealed a nanoscale, layered flake-like morphology that is advantageous for improved electrochemical performance. Nitrogen adsorption–desorption (BET) analysis confirmed a mesoporous structure with a high accessible surface area. Furthermore, X-ray photoelectron spectroscopy (XPS) was used to analyze the surface composition and oxidation states, confirming the presence of cerium, cobalt, and oxygen species within the composite.

Electrode Preparation

Electrochemical testing was performed using electrodes prepared by coating the synthesized material onto a conductive substrate. The electrode slurry was formulated by mixing the active material, carbon black, and polyvinylidene fluoride (PVDF) binder in an 85:10:5 mass ratio, with N-methyl-2-pyrrolidone (NMP) used as the solvent to produce a uniform paste. This mixture, with a mass loading of approximately 2.5 mg cm^{-2}, was evenly applied onto pre-treated nickel foam (1 × 2 cm^2). Before coating, the nickel foam was cleaned with dilute HCl and thoroughly rinsed with deionized water to remove surface contaminants. The coated electrodes were then dried at 70 °C for 4 h to ensure complete solvent evaporation and strong adhesion of the active layer. Electrochemical measurements were conducted in 2 M KOH electrolyte using a three-electrode setup, where the coated nickel foam served as the working electrode, a platinum wire acted as the counter electrode, and a Hg/HgO electrode functioned as the reference. Cyclic voltammetry (CV), galvanostatic charge–discharge (GCD), and electrochemical impedance spectroscopy (EIS) were employed to evaluate the electrochemical performance. The specific capacity (Ah g^{-1}) derived from CV curves was calculated using Equation **1**.

$$C = \frac{\int I(V)\, dV}{3600 * m\nu} \quad (1)$$

Here, ν (V s^{-1}) denotes the scan rate, m (g) represents the mass of the active material, and ΔV (V) corresponds to the potential window. The specific capacity (Ah g^{-1}) obtained from the GCD profiles was calculated using Equation (2).

$$C_{sp} = \frac{\int idt}{3600 * m} \quad (2)$$

Here *i* (A) denotes the discharge current, *t* (s) represents the discharge time, *m* (g) corresponds to the mass of the active material, and *V* (V) indicates the potential window after excluding the IR drop. Electrochemical impedance spectroscopy (EIS) was performed across a frequency range of 0.01 Hz to 100 kHz using a small AC perturbation amplitude. This analysis enabled the determination of internal resistance (R_s), charge-transfer resistance (R_{ct}), and ion diffusion behaviour.

Device Fabrication

An hybrid solid-state supercapacitor was assembled using the $Gd(OH)_3$–MXene composite as the positive electrode and activated carbon (AC) as the negative electrode, with a PVA/KOH gel serving as the solid electrolyte. The AC electrode was prepared following the same procedure used for the positive electrode. To maintain charge balance between the two electrodes, the mass loading of the active materials was adjusted according to the charge-matching principle. The gel electrolyte was produced by dissolving 1 g of polyvinyl alcohol (PVA) and 1 g of KOH in 10 mL of deionized water under continuous stirring at 80 °C until a clear, homogeneous gel formed, which was then allowed to cool to room temperature. For device fabrication, the gel electrolyte was uniformly applied to both electrodes and left to dry for about 2 h to ensure strong interfacial adhesion. The electrodes were then placed face-to-face with a filter-paper separator between them, and the entire assembly was tightly wrapped with Teflon tape to enhance mechanical stability and prevent electrolyte leakage. The completed asymmetric solid-state supercapacitor was subsequently subjected to detailed electrochemical evaluation. The performance of both the individual electrodes and the full device was analysed using standard equations to calculate specific capacitance (F g^{-1}), energy density (Wh kg^{-1}), and power density (W kg^{-1})

$$E = \frac{CV^2}{2 * 3.6} \quad (3)$$

$$P = \frac{E * 3600}{\Delta t} \quad (4)$$

XPS analysis

The surface chemistry and electronic structure of the $Gd(OH)_3$–$Ti_3C_2T_x$ composite were examined using XPS. The wide-scan survey spectrum demonstrated in **Figure S1 (a)** confirms the presence of Gd, Ti, C, and O elements, verifying the successful formation of the composite without detectable impurities. The C 1s spectrum shown in **Figure S1 (b)** can be resolved into components associated with C–Ti (~281–282 eV), C–C/C=C (~284.6 eV), and C–O (~286–288 eV) bonds [1], further confirming the presence of $Ti_3C_2T_x$ MXene along with oxygen-containing functional groups. Finally, the O 1s spectrum (**Figure S1 (c)**) shows signals from lattice oxygen in Gd–O bonds, hydroxyl groups, and oxygen-based surface terminations of MXene. The overlap of these oxygen species highlights strong interfacial interactions between $Gd(OH)_3$ and $Ti_3C_2T_x$, reinforcing the composite's integrated

structure. The Ti 2p spectrum shown in **Figure S1 (d)** exhibits Ti $2p_3/_2$ and Ti $2p_1/_2$ peaks in the ranges of ~455–459 eV and ~461–465 eV, respectively[2]. The high-resolution Gd 3d spectrum (**Figure (e)**) shows two distinct peaks at binding energies of ~141.3 eV and ~147.6 eV, corresponding to the Gd $4d_5/_2$ and Gd $4d_3/_2$ spin–orbit components [3]. These values are consistent with Gd^{3+} species in gadolinium hydroxide, confirming the oxidation state and chemical environment of Gd in the composite. Deconvolution reveals contributions from both Ti–C and Ti–O bonds, originating from the $Ti_3C_2T_x$ MXene framework and surface terminations (–O, –OH, –F). This indicates that the MXene maintains its chemical identity while interacting with the $Gd(OH)_3$ phase.

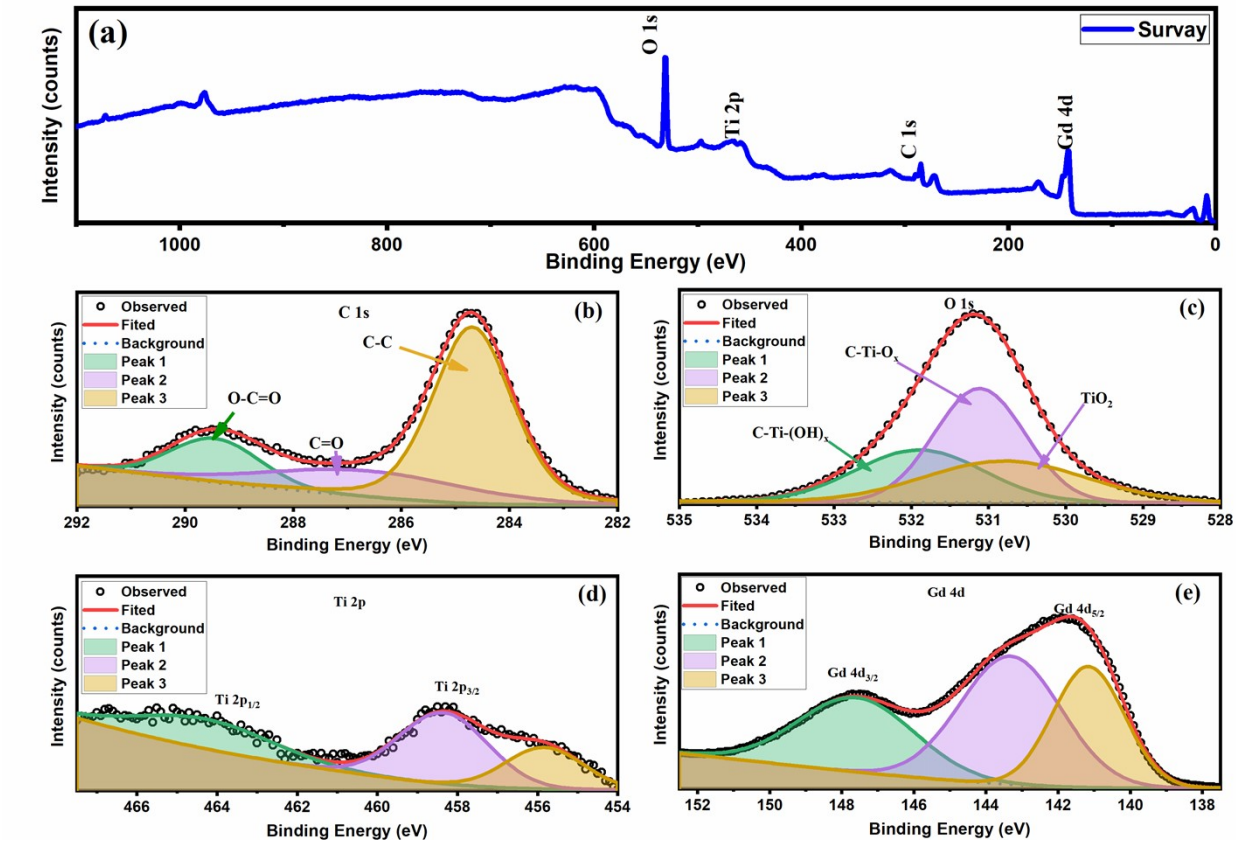

Figure S1 XPS analysis of the $Gd(OH)_3$–MXene nanocomposite: **(a)** survey spectrum, and core-level spectrum of **(b)** C 1s **(c)** O 1s **(d)** Ti 2p and **(e)** Gd 4d.

EIS comparison

Fig. S2 presents the Nyquist plots of $Gd(OH)_3$ and Gd–MXene electrodes. Compared with pristine $Gd(OH)_3$, the Gd–MXene electrode shows a reduced solution resistance, suggesting improved electrical conductivity after MXene incorporation. The conductive MXene sheets may facilitate faster electron transport and enhance the overall conductive network of the $Gd(OH)_3$-based electrode, thereby improving its electrochemical performance.

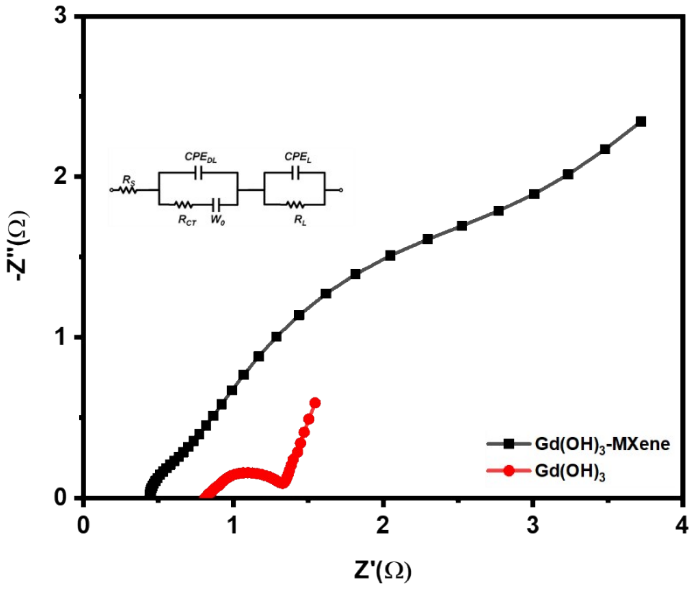

Fig. S2 Nyquist plot for $Gd(OH)_3$ and $Gd(OH)_3$-MXene

Table S1 Comparative electrochemical performance of $Gd(OH)_3$-MXene with previously reported materials.

Material	Synthesis method	Electrode performance	Device performance	Ref.
CNF/Gd_2O_3	Electrospinning and carbonization	NA	Energy Density of 8.12 Wh kg^{-1} and Power density of 300 W kg^{-1}, retention of 97% of initial capacity after 10000 cycles	[4]
$Gd(OH)_3$-DNA-60	Facile precipitation method	Specific capacitance of 576.6 Fg-1 at 1 Ag-1	Energy density of 29.3 Wh kg^{-1} and power density of 799.6 W kg^{-1}, capacitance retention of 95% after 10000 cycles	[5]
Gd^{3+} doped $V_2O_5/Ti_3C_2T_x$ MXene	Wet chemical approach	Specific capacitance of 1024 F g^{-1} at 10 mVs^{-1}	NA	[6]
Gd_6MoO_{12}	Sonochemical method	Specific capacitance of 156.27 F g^{-1} at 1 Ag^{-1}	NA	[7]
$GdVO_4$	Microwave-assisted hydrothermal method	Specific capacitance of 1203.75 F g^{-1} at 1 Ag^{-1}	Energy Density of 130.2 Wh kg^{-1} and Power density of 2880.18 W kg^{-1}	[8]
Gd(OH)-MXene	Microwave Assisted	Specific capacitance of 924 F g^{-1} at 1.5 Ag^{-1}	Energy Density of 25.8 Wh kg^{-1} and Power density of 3000 W kg^{-1}	

References

1 P. E. Lokhande, V. Kadam, C. Jagtap, U. Rednam, N. Lakal and B. A. Al-Asbahi, *Diamond and Related Materials*, 2025, **154**, 112191.

2 V. Natu, M. Benchakar, C. Canaff, A. Habrioux, S. Célérier and M. W. Barsoum, *Matter*, 2021, **4**, 1224–1251.
3 N. Ullah, M. Imran, K. Liang, C.-Z. Yuan, A. Zeb, N. Jiang, U. Y. Qazi, S. Sahar and A.-W. Xu, *Nanoscale*, 2017, **9**, 13800–13807.
4 H. Aydın, B. Üstün, Ü. Kurtan, A. Aslan and S. Karakuş, *ChemElectroChem*, 2024, **11**, e202300585.
5 J. Yesuraj, J. Kim, R. Yang and K. Kim, *Adv Compos Hybrid Mater*, 2024, **7**, 69.
6 T. Tahir, D. Alhashmialameer, S. Zulfiqar, A. M. E. Atia, M. F. Warsi, K. Chaudhary and H. M. El Refay, *Ceramics International*, 2022, **48**, 24840–24849.
7 Z. Pekdemir, F. K. Dokan, M. S. Onses and E. Sahmetlioglu, *ChemistrySelect*, 2026, **11**, e05571.
8 F. J. S. Barros, K. L. P. Cardoso, E. Longo, A. A. Tanaka, M. A. S. Garcia and I. M. Pinatti, *J Mater Sci*, 2023, **58**, 15459–15470.